APPLIED PHYSICS

Polyelectrolyte-based wireless and drift-free iontronic sensors for orthodontic sensing

Jia Song[1]†, Rusong Yang[2]†, Junli Shi[1], Xingxing Chen[1], Sai Xie[1], Zelong Liao[1], Ruijie Zou[1], Yupeng Feng[2], Terry Tao Ye[2]*, Chuan Fei Guo[1]*

Copyright © 2025 The Authors, some rights reserved; exclusive licensee American Association for the Advancement of Science. No claim to original U.S. Government Works. Distributed under a Creative Commons Attribution NonCommercial License 4.0 (CC BY-NC).

The real-time monitoring of health conditions of humans is a long-lasting topic, but there are two major challenges. First, many biomedical applications accept only implanted sensors. Second, tissue-like soft sensors often suffer from viscoelasticity-induced signal drift, causing inaccurate measurements. Here, we report a wireless and drift-free sensory system enabled by a low-creep polyelectrolyte elastomer. The system consists of the iontronic pressure sensors incorporating inductance-capacitance (LC) oscillators, exhibiting combined low drift ratio, high *Q* factor, high robustness to interferences, and wide-range measurement, superior to other capacitive sensors using regular dielectrics or ionogels. We have recorded 14-day orthodontic loads of two subjects using the system, showing pressure decreasing from 300 to 50 kPa and torque from 12.5 to 0.5 N·mm. The wireless, drift-free sensory system may be extended to other implants for long-term and accurate sensing.

INTRODUCTION

Developing implanted sensors to monitor pressure or other physiological signals is a promising technology for advanced health care (*1*, *2*). Sensors have been implanted in vessels to detect blood pressure (*3*, *4*), in joints to detect the intraarticular pressure (*5*), and on hearts to record electrocardiographic signals (*6*–*8*). Besides subcutaneous implants, sensors may also be implanted in the intraoral environment. Malocclusion is a prevalent dental health problem that affects both chewing functionality and aesthetic appearance and is often treated using tooth aligners, which straighten teeth by imposing a prolonged pressure (for overbite), sometimes together with a torque (for crossbite) (Fig. 1A) (*9*). The continuous monitoring of orthodontic pressure and torque can evaluate the effect of treatment using an aligner. Although a variety of methods or tools including mises strain test (*10*), pressure films (*11*), and six-axis orthodontic force and moment sensing systems (*12*) are available for orthodontic load detection, they often face the challenge of installing complicated and stiff sensors and wired signal connection.

Flexible pressure sensors in the format of a thin layer can be deployed between the tooth surfaces and the inner surface of an aligner (*13*). However, the soft active materials in flexible sensors easily creep under prolonged high stresses because of their intrinsic viscoelasticity, causing signal drift and inaccurate measurement (*14*). Signal drift is a substantial issue for orthodontic load measurements because of the high (100-kPa level) and prolonged (many days) load imposed to teeth. Among many types of flexible pressure sensors, iontronic sensors are an ideal selection presenting advantages of wide-range high sensitivity to static pressure (*15*). Nevertheless, viscoelasticity-induced creep aside, ionogels—the most widely used active materials in iontronic sensors—have an additional issue of ion leakage (*14*, *16*), which leads to enhanced signal drift and potential biosafety risk to humans. Few ionic materials are creep-free while they cannot be mass produced (*14*). Another challenge in orthodontic load measurement lies in the in vivo wireless sensing of multiple teeth. Passive wireless sensing (*16*–*24*) is a preferable solution for orthodontic stress testing, while the coupling of the wireless circuit with the iontronic sensor, particularly the effect of ion dissociation state of ionic materials on sensing properties, is still unclear.

Here, we propose an inductance-capacitance (LC) orthodontic sensing system (LCOSS) for wireless and real-time orthodontic pressure and torque measurement. The system uses flexible iontronic capacitive sensors based on a low-creep and leakage-free polyelectrolyte for drift-free pressure/torque sensing (Fig. 1, B and C), in combination with near-field inductive coupling for wireless signal transmission. This polyelectrolyte-based sensor presents advantages of a high pressure resolution of 1%, a low drift ratio < 2%, a high *Q* factor of 54, and high immunity to interferences. We show that polyelectrolytes are desired materials for wireless LC sensors—other capacitive sensors, including those based on ionogels or soft dielectrics, are dissatisfactory either in signal quality or in sensing capability. Our sensor also exhibits high biocompatibility to enable safe and in vivo implants in an intraoral environment. The LCOSS integrated to an aligner detects orthodontic pressure variation from 300 to 50 kPa and torque from 12.5 to 0.5 N·mm during a 14-day orthodontic treatment of two subjects. The LCOSS is expected to have many other applications that require wireless and accurate pressure sensing.

RESULTS

Design of the LC orthodontic sensing system

The LCOSS consists of an array of LC sensors embedded in an aligner, along with wireless testing hardware and software (fig. S1). A flexible LC pressure sensor and an LC torque sensor were designed for the sensor array, with each sensor covering an area of 6 mm by 6 mm. Each LC sensor consists of one or two pressure-sensitive capacitor and a coupling coil to form an LC resonator and encapsulated in a protective layer of polydimethylsiloxane (PDMS) (Fig. 1D), which is conformal to the curved surfaces of teeth (Fig. 1E).

The pressure-sensitive capacitor of an LC sensor consists of two flexible electrodes of polyimide-copper (PI-Cu) sandwiching a microstructured polyelectrolyte layer. This polyelectrolyte material can

[1]Department of Materials Science and Engineering, Southern University of Science and Technology, Shenzhen 518055, P. R. China. [2]Departmen of Electrical and Electronic Engineering, Southern University of Science and Technology, Shenzhen 518055, P. R. China.
*Corresponding author. Email: yet@sustech.edu.cn (T.T.Y); guocf@sustech.edu.cn (C.F.G.)
†These authors contributed equally to this work.

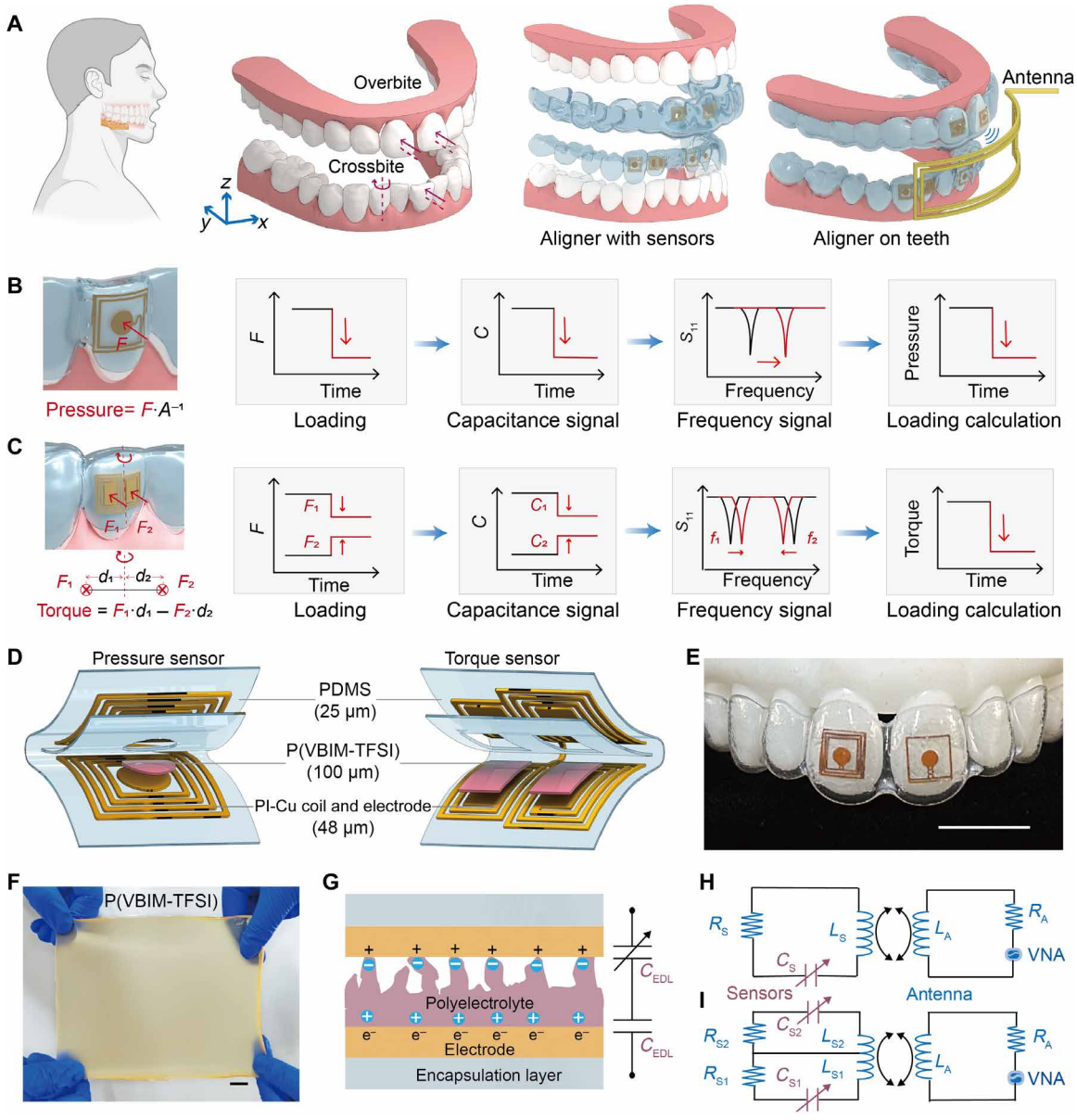

Fig. 1. Principle of the LC orthodontic pressure and torque testing system. (**A**) Schematic of the wireless sensors embedded in an aligner for orthodontic load test. (**B** and **C**) Principle of orthodontic pressure and torque sensing. Orthodontic force (*F*) causes a change in the sensor's capacitance (*C*) and thereby a shift in resonant frequency f_r, determined by the position of the local minimums in reflection coefficient (S_{11}) spectrum. The parameters of area (*A*) and distances (d_1 and d_2) in the equations are constants, and F_1 and F_2 are forces applied on the two parts of the tooth. (**D**) Schematic diagram of the LC sensors. (**E**) Photograph of two sensors attached to a teeth model. Scale bar, 1 cm. (**F**) Large-area preparation of polyelectrolytes. Scale bar, 1 cm. (**G**) Principle of the capacitor for pressure sensing based on the interfacial electric double layer. (**H** and **I**) Schematic diagram of inductive coupled (H) pressure sensing and (I) torque sensing. Resonant frequencies of the LC sensors are measured wirelessly via a vector network analyzer using an external reading antenna through inductive coupling. In the diagram, R_A, R_S, R_{S1}, and R_{S2} are the resistances; L_A, L_S, L_{S1}, and L_{S2} are the inductances; and C_S, C_{S1}, and C_{S2} are the capacitances with the subscripts S and A representing the sensor and the antenna, respectively. Subscripts S1 and S2 represent the two parallel-connected LC circuits (see Supplementary Text for details). VNA, vector network analyzer.

be mass-produced in a photocuring polymerization process (Fig. 1F and fig. S2). An electric double layer (EDL) is formed between the electronic conductor (PI-Cu electrode) and the ionic conductor (polyelectrolyte) (Fig. 1G). A pressure applied to the sensor will lead to the change in contact area between the electrode layer and thereby the change of capacitance of the EDL (*25*, *26*). Two types of LC sensors were designed to measure the change in orthodontic pressure and torque. The LC pressure sensor features a single capacitor suitable for normal stress detection (Fig. 1H), and the LC torque sensor incorporates two pressure-sensitive capacitors, measuring the forces at two separate parts, and the torque measurements can be extracted from the forces and the distance between the capacitors (Fig. 1I).

The resonant frequency f_r of an LC circuit defined as $f_r = \frac{1}{2\pi\sqrt{LC}}$, which can be detected through inductive coupling, where L and C are the inductance and capacitance of the sensor, respectively. It is essential to differentiate the resonant frequencies of the sensors for real-time and simultaneous measurement of multiple LC sensors. Given that high-frequency signals are susceptible to interference and parasitics (*27*–*29*), the range of f_r of the sensors needs to be calibrated within the gigahertz range, with lower frequencies being more desirable (*30*, *31*). The capacitance of the sensor is proportional to the contact area between the electrode and ionic material (or the area of EDL interface) and also affected by the species of ions used (*25*, *32*), and the inductance is determined by the coupling coil structure. By optimizing the design, we achieved a series of LC sensors with the resonance frequency ranging from 100 MHz to 2 GHz.

Synthesis, mechanical, and electrical properties of the polyelectrolyte

We used a creep- and leakage-free polyelectrolyte as the ionic conductor for the capacitors of the LC sensors. Polyelectrolytes are ionic materials for which cations or anions are engrafted to the polymer chains without ion leakage (*33*). Creep of a polymer is a slow deformation or rearrangement of polymer chains when subjected to prolonged high pressure, often related to the viscoelasticity of the material (*34*). Here, we designed and synthesized a polyelectrolyte incorporating dense crosslinks with charged molecular chains to form a network. Specifically, we polymerized 1-vinyl-3-butylimidazolium bis(trifluoromethylsulfonyl) imide ([VBIM][TFSI]) with a crosslinker of triethyleneglycol divinyl ether (TDE) into a soft elastomer, denoted as P(VBIM-TFSI).

We show that without crosslinking, P(VBIM-TFSI) is in a glassy state (Fig. 2A), with a Young's modulus of 130 MPa. When adding 20 weight % (wt %) TDE during polymerization, the material becomes much softer (Fig. 2, A and B, and fig. S3), and the Young's modulus decreases to 6.5 MPa along with an elongation at break of 60% (Fig. 2, C and D). The Young's modulus of the polyelectrolyte decreases as crosslinking density increases because of the decreased degree of crystallinity and the high flexibility of the ether bonds in the crosslinker (fig. S4). The results show that TDE can effectively soften P(VBIM-TFSI) to impart appropriate elasticity and stretchability.

Engineering the molecular structure of P(VBIM-TFSI) results in negligible creep. Besides the role played by TDE with ether bonds, the high crosslinking density (with 20 wt % crosslinkers) can decrease the polymer chain length and reduce interchain frictions to suppress its creep, while the glassy polymer is softened by destroying the crystalline structure with the crosslinkers. We show that at a pressure of 300 kPa, the compressive strain changes from 20.47 to 21.13% over 10 hours, with a minimal change of only 0.66%. Specifically, the strain level is almost unchanged after loading for 4 hours (Fig. 2E).

We further measured the electrical conductivity of the crosslinked polyelectrolyte elastomer. The ionic conductivity rises from 1.6×10^{-8} S·cm^{-1} for noncrosslinked P(VBIM-TFSI) to 4.3×10^{-6} S·cm^{-1} for the heavily crosslinked P(VBIM-TFSI) (Fig. 2F and fig. S5). The increase of ionic conductivity is attributed to the increase of the free volume between molecular chains and the decrease of the glass transition temperature (fig. S6) (*35*–*37*). The high ionic conductivity can help achieve high sensitivity of sensors, increase the capacitance of the EDL, and decrease the minimum frequency of the LC circuit for a better tolerance to interference.

Sensing properties and signal drift behavior

The pressure sensing capability of the LC sensor is determined by the pressure-sensitive capacitor (or pressure sensor). We measured the capacitance-to-pressure response of the sensor, exhibiting linear response with sensitivity (S) of 7.3 pF·kPa^{-1} over a pressure range of 0 to 600 kPa (Fig. 3A). This range covers the common orthodontic pressures during tooth straightening. The sensor also exhibited stable response in both capacitance and f_r under stepwise pressure change from 50 to 80 kPa (Fig. 3B). We used two parameters, drift ratio and drift rate (*14*), to quantitatively assess the stability of signals under static pressures. Drift ratio is defined as the relative change in signal magnitude when loading a pressure over a certain period, and drift rate is the rate of drift ratio over time. We assessed a batch of sensors, and they exhibited a low drift ratio $< 2\%$ at 300 kPa over 10 min and a maximum drift rate of 0.3% min^{-1} (Fig. 3C). By contrast, a control sensor that replaces the polyelectrolyte with an ionogel of 1-ethyl-3-methylimidazolium bis(trifluoromethylsulfonyl)imide–infused poly(vinylidene fluoride-*co*-hexafluoropropylene) {(PVDF-HFP)-[EMIM][TFSI]}, a commonly used active material for iontronic sensors, exhibits a drift ratio of 30% and a maximum drift rate of 80% min^{-1}.

The drift rate of our polyelectrolyte-based sensor decreases with time, and eventually no drift is observed after loading for 10 min (fig. S7). Therefore, our polyelectrolyte-based sensor is suitable for long-term tests. In Fig. 3D, we show that a sensor has negligible drift in both capacitance (from 2.032 to 2.158 nF) and f_r (from 362.6 to 362.1 MHz) under 300 kPa over 10 hours. The low drift ratio of the capacitor can maintain under different test frequencies of 1, 10, and 100 kHz (Fig. 3E and fig. S8). In comparison, the ionogel-based control sensor shows a drift in capacitance by 48% and a drift in f_r by 20% under 300 kPa in only 10 min (Fig. 3F and fig. S9), and signal drift occurs at various test pressure (Fig. 3G). In addition, the polyelectrolyte-based sensor is also humidity-stable, and minor change of the sensor response occurs over 8 hours by varying the relative humidity from 45 to 85% (fig. S10). This is because of the hydrophobic nature of the polyelectrolyte elastomer and the encapsulation using PDMS.

In addition to signal drift, the resonant frequencies of LC sensors may be affected by the background noise and interferences from the environment such as parasitic capacitance and inductance. We use two indices, Q factor and signal-to-interference ratio (SIR), to evaluate the quality and anti-interference behavior of the LC sensor signals. Q factor represents the ratio of stored energy to dissipated energy of a circuit during measurement (movies S1 and S2, and fig. S11). A signal with a higher Q factor has a sharper local minimum in S_{11} spectrum for easier identification of the f_r. Note that the Q factor decreases with the magnitude of load because it follows $Q = \frac{1}{R}\sqrt{\frac{L}{C}}$, where R is the resistance. That means the noise level increases when loaded. SIR is a measure that evaluates the degree of ease of a system to be interfered.

In our experiment, we compared our polyelectrolyte-based LC sensor with two control sensors: an ionogel-based LC sensor using (PVDF-HFP)-[EMIM][TFSI] and a dielectric-based LC sensor using a soft ion-free material PDMS. Our results show that the polyelectrolyte-based sensor and the PDMS-based sensor both have a high Q factor of 54 and 76, respectively, while the ionogel-based sensor, although being highly sensitive to pressure, exhibits a very low Q factor of 8.6 and is not suitable for an LC sensor, let alone

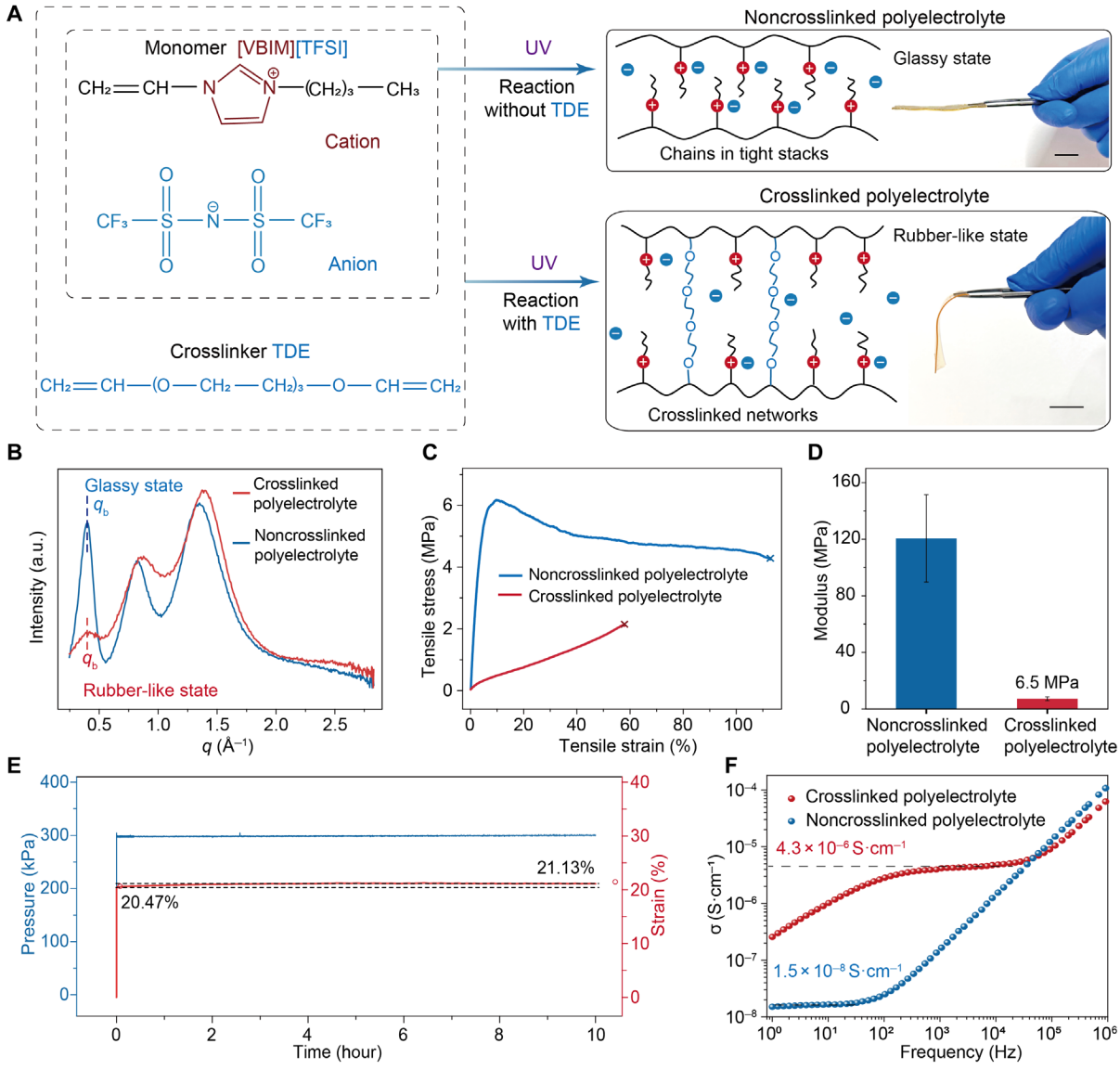

Fig. 2. Synthesis, mechanical properties, and electrical conductivity of the crosslinked P(VBIM-TFSI) polyelectrolyte. (**A**) Synthetic route and crosslinking modification of P(VBIM-TFSI) polyelectrolyte. The inset shows that the noncrosslinked polyelectrolyte is hard, whereas the crosslinked polyelectrolyte is soft and looks like a rubber. Scale bars, 1 cm. (**B**) Wide-angle x-ray scattering spectra of the noncrosslinked polyelectrolyte and the crosslinked polyelectrolyte. q_b represents the scattering vector between backbones, with a corresponding correlation distance d_b given by the relation $d_b = 2\pi / q_b$ (see fig. S3 for details). (**C**) Tensile stress-strain curves of the two polyelectrolytes. (**D**) Young's modulus of the two polyelectrolytes. (**E**) Creep test of the crosslinked polyelectrolyte under a constant compressive stress of 300 kPa. (**F**) Electrical conductivity as a function of frequency for the crosslinked polyelectrolyte and noncrosslinked polyelectrolyte.

the ion leakage-caused signal drift. The poor Q factor of ionogel-based sensor stems from the high dielectric loss of ionogels (fig. S12), which is caused by strong ionic polarization (*38*, *39*) and interface polarization (*40*) in an electromagnetic field. By contrast, in a polyelectrolyte, most ions are disassociated and trapped in polymer chains, little energy is dissipated by ionic polarization, and the polyelectrolyte-based sensor exhibits a high Q factor close to that of PDMS-based sensors. The relationship between Q factor and dielectric loss tangent is expressed as $Q = 1 / \tan \delta$ (*41*). The PDMS-based sensor exhibits a high Q factor due to its low dielectric loss (fig. S12). However, its small capacitance makes it unsuitable for many applications.

The polyelectrolyte-based sensor is superior to the dielectric (PDMS)–based sensor in terms of a wider working range and a higher SIR. The PDMS-based sensor exhibits signal saturation at 60 kPa or higher (fig. S13), with a small change in capacitance (~1.0 pF) and smaller $\Delta f/f_0$ (where the Δf is the frequency difference before and after loading and f_0 is the initial frequency) of 2% over full scale. Note that the limited pressure-response range (<60 kPa) of the PDMS-based LC sensor is inadequate for orthodontic pressure measurement (requiring at least 0 to 300 kPa). By contrast, the polyelectrolyte-based LC sensor has a wide working range of 0 to 650 kPa, with a thousand-fold change in capacitance from 4 to 4010 pF. The large change in capacitance results in a large normalized change

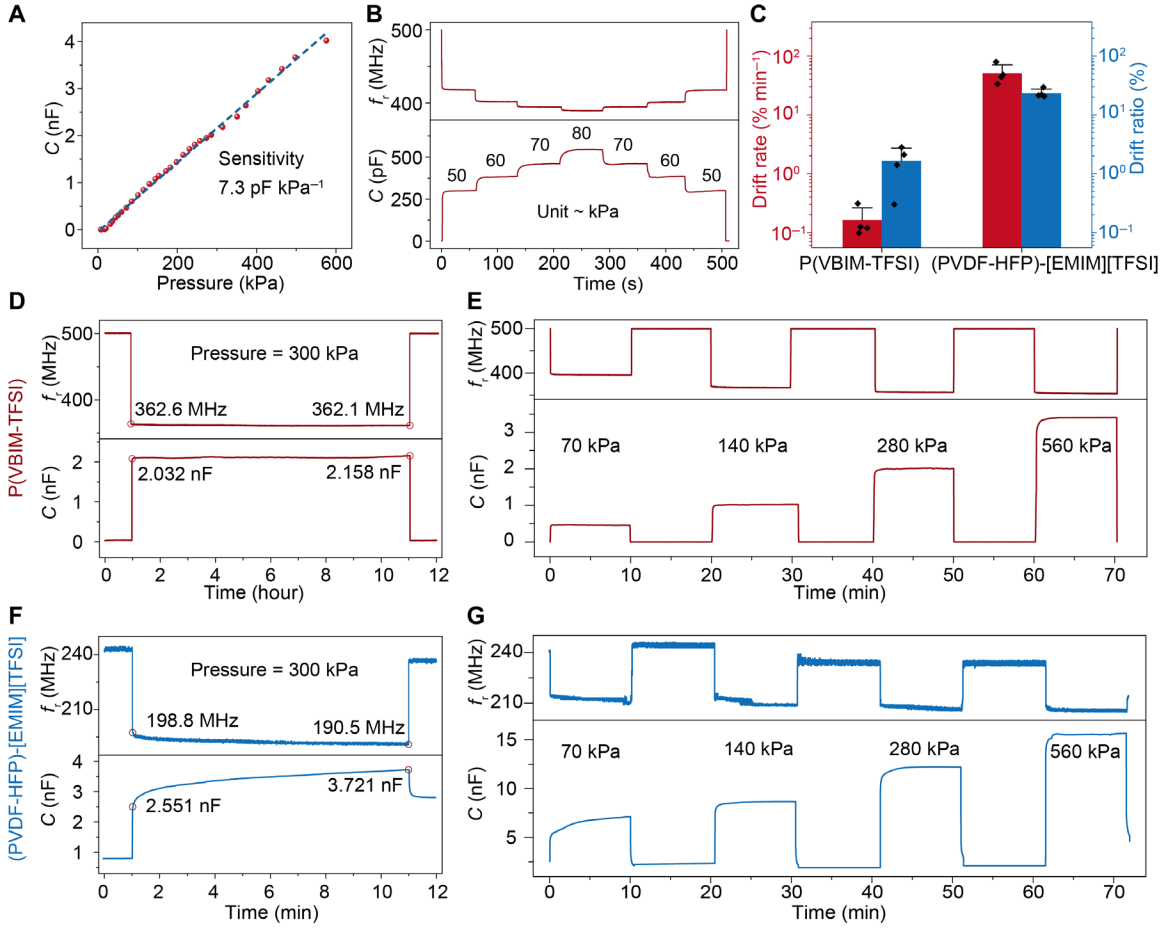

Fig. 3. Sensing properties and drift behavior of the polyelectrolyte-based pressure sensor. (**A**) Capacitance as a function of pressure for the polyelectrolyte-based capacitor. (**B**) Dynamic tracking of resonant frequency and capacitance in response to pressure steps. (**C**) Drift rate and drift ratio of the capacitors based on polyelectrolyte and ionogel. (**D**) Capacitance and resonant frequency of the polyelectrolyte-based sensor under a static pressure of 300 kPa for 10 hours. (**E**) Capacitance and f_r curves of the polyelectrolyte-based sensor under pressures of 70, 140, 280, and 560 kPa over 10 min for each pressure. (**F**) Capacitance and resonant frequency of the ionogel-based sensor under a static pressure of 300 kPa for 10 min. (**G**) Capacitance and f_r curves of the ionogel-based sensor under pressures of 70, 140, 280, and 560 kPa over 10 min for each pressure.

in frequency ($\Delta f / f_0$) following the relation $f \sim C^{-1/2}$. Moreover, the polyelectrolyte-based sensor exhibits a higher SIR of 49 dB than that of the PDMS-based sensor (31 dB) (fig. S14). This is because the small $\Delta f / f_0$ causes a low precision for measurement. Higher SIR suggests that the polyelectrolyte-based sensor is more robust to environmental interferences. A performance comparison of the developed polyelectrolyte-based wireless sensing system with previously reported passive systems is presented in table S1.

Wireless sensory system and its performances

Each LC sensor in a sensory array has a specifically distinctive design, e.g., different loops of coils, for simultaneous readout of multiple sensors. When coupled with multiple LC sensors with each sensor having a specific f_r, the input reflection coefficient [S_{11} parameter, measured using a vector network analyzer (VNA)] spectrum of the reading antenna exhibits several local minimums corresponding to the resonant frequencies of the sensors (Supplementary Text and fig. S15). As a result, the multiple LC sensors can be measured simultaneously without cross-talk. We varied the number of the coupling coil loops to generate substantially different resonant frequencies and designed 12 different LC pressure sensors with series number from #1 to #12 that resonate at different frequencies spanning from 200 MHz to 1.2 GHz, and they are deployed in an order from the highest f_r to the lowest (Fig. 4A and fig. S16). Moreover, a preferred range of resonant frequency for our system is between 200 and 800 MHz due to the steady dielectric loss (fig. S12) and a limited sensor size. Double-sided inductive coils were used to increase the inductance while maintaining a small form factor. The coupling coils of one LC circuit were looped in an opposite direction to enhance their mutual inductance, rather than cancellation (*3*).

The responses of the LC sensors were simulated using Ansys high-frequency structure simulator (HFSS) software and experimentally measured using a VNA (fig. S17). Taking sensor #12 for example, our experiment shows that its resonance frequency shifts from 262 to 148 MHz as the pressure (P) increases from 0 to 512 kPa (Fig. 4B). We further measured the f_r-P curves of the sensors to calibrate the applied pressure on teeth (Fig. 4C and fig. S18). Furthermore, this sensor exhibits a high pressure resolution of 1 kPa (or 1%) at a base pressure of 100 kPa, and a decrease of the resonant frequency from 178.4 to 177.7 MHz is measured with the increase of the pressure of 1 kPa (Fig. 4D).

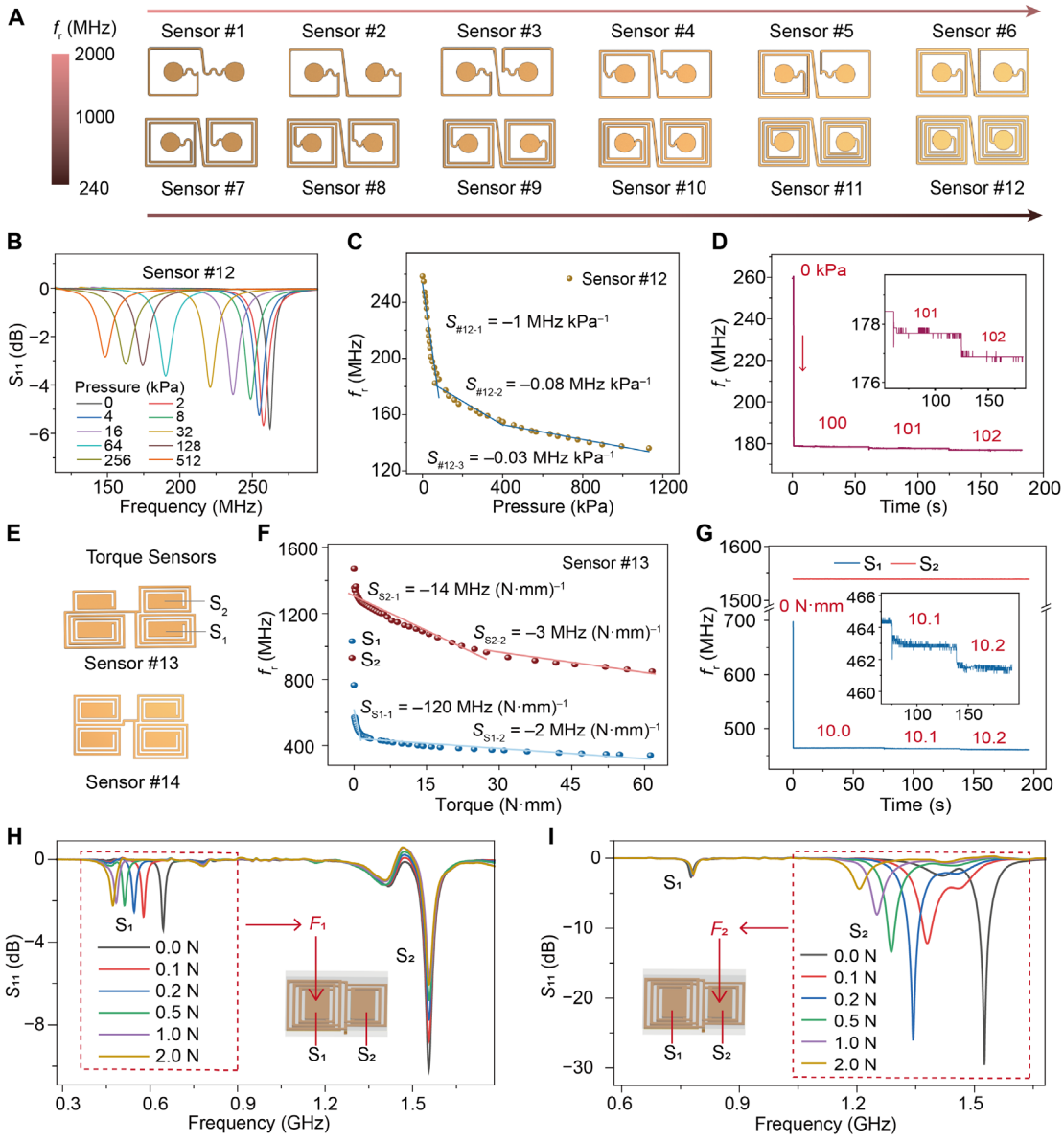

Fig. 4. Design and properties of the LC sensor array for pressure and torque sensing. (**A**) Structures of the LC pressure sensor circuits with different resonant frequencies f_r, which decrease as the number of coils increases. (**B**) Measured S_{11} parameter to frequency under different pressures of sensor #12. (**C**) Resonant frequency as a function of pressure of sensor #12. (**D**) Resonant frequencies of sensor #12 under loads of 100, 101, and 102 kPa. (**E**) Structures of the LC torque sensor. (**F**) Resonant frequency as a function of torque for sensor #13. (**G**) Resonant frequencies of sensor #13 under loads of 10.0, 10.1, and 10.2 N·mm. (**H** and **I**) Results showing that the torque sensor is cross-talk-free. A torque sensor consists of two parts: S_1 and S_2. When applying different loads on S_1, no change in f_r is observed for S_2 and vice versa.

In addition to the LC pressure sensors, we also designed and fabricated two LC torque sensors, numbered as #13 and #14 (Fig. 4E), which consist of two pressure-sensitive capacitors connected in parallel and deployed horizontally on the two halves of a tooth, and the resonance of the circuit is verified by simulation and experiment (fig. S19 and movie S3). Similar to the LC pressure sensor, taking sensor #13 for example, f_r of the sensor as a function of torque is measured to calibrate the applied torque on teeth (Fig. 4F), and this sensor exhibits a torque resolution of 0.1 N·mm (or 1%) at a base torque of 10 N·mm (Fig. 4G). The LC torque sensors exhibit minimal cross-talk, and the resonant frequencies of the two capacitors vary independently (Fig. 4, H and I, and fig. S20). Moreover, we also tested a series connected torque sensor configuration in comparison, but the design exhibits severe cross-talk (fig. S21).

In vivo orthodontic pressure and torque measurement

For orthodontic pressure and torque tests, a MATLAB application was developed to monitor and analyze the spectrum of S_{11} parameter. This application can calculate the spectra difference before and after the reading antenna approaches the sensor to eliminate the interference and can also uses Gaussian curve fitting (*42*) method to distinguish the resonant frequencies when they overlap (fig. S22). We first conducted experiments on tooth models before test. A curved reading antenna conformal to the aligner was used for the

test to ensure effective coupling. We show that the wireless signals can be used to identify the six sensors embedded in the aligner simultaneously. Furthermore, in the case of gradient displaced overbite and crossbite tooth models, gradient orthodontic pressure and torque results compliant with the displacements were acquired (fig. S23 and movies S4 to S6).

The cytocompatibility of the sensor was assessed by incubating human adult fibroblasts (HAFs) and human umbilical vein endothelial cells (HUVECs) with a sensor for 24 hours. Fluorescence staining results demonstrated that HAF cells attached well to the surface of the sensor. Furthermore, quantitative analysis using Cell Counting Kit-8 assay showed the proliferation of HUVEC cells with 100% viability in both the control group and the sensor group during 24-hour monitoring (fig. S24). All the results indicate desired biocompatibility of the sensor because the sensor is encapsulated in PDMS, and the polyelectrolyte is leakage-free to ensure its biosafety.

We conducted real-time wireless pressure sensing in a subject (subject A) with deep overbite (Fig. 5, A and B) and torque sensing in another subject (subject B) with crossbite (Fig. 5C). The orthodontic pressure of subject A was recorded each day over a period of 14 days using a portable nanoVNA system–based LCOSS (Fig. 5A and fig. S25). Figure 5D shows the picture of the subject wearing an LC pressure sensor on an incisor. The resonant frequencies of the LC pressure sensors were recorded during the in vivo test (Fig. 5E) and then converted into pressure values (Fig. 5F and figs. S26 and S27). The two incisors of subject A were moved inward by 100 μm during the treatment, and accordingly, the measured orthodontic pressure dropped from the initial value of 300 to ~50 kPa after 14 days (movie S7). The measured orthodontic pressure can be used as the input to simulate and analyze the stress condition of the teeth and alveolar bone, and the results show that the stress imposed to the alveolar bone relieves from 1 MPa to 200 kPa during the test (Fig. 5G and fig. S28).

For subject B, an incisor was rotated by 2° along the middle axis during the 14-day test. The torque on the tooth decreased during the treatment, measured from the initial value of 12.5 to only 0.5 N·mm in day 14 (Fig. 5, H to J, and movie S8). Accordingly, there is also a stress relief on the alveolar bone—the initial stress was about 500 kPa in the first 3 days and gradually decreased to ~50 kPa after 14 days (Fig. 5K). The decreases of the stress in the tests are primarily attributed to the root absorption that enables the movement and rotation of the teeth. The pressure and torque measurement provide a clear understanding on the dynamic biomechanical information during orthodontic treatments.

DISCUSSION

We have demonstrated wireless pressure and torque measurement based on iontronic LC sensors, a class of emerging sensing devices based on soft ionic materials. The use of low-creep and leakage-free polyelectrolyte enables sensing with an adequate pressure resolution, a wide working range, and high stability of the signal in long-term measurement. Our study shows that polyelectrolyte is a desired active material for LC pressure sensing. Drift-free (0.4% drift ratio in f_r) and wide-range sensing aside, it also provides signals with a high Q factor, a high SIR, and a large detectable change in f_r. By contrast, ionogel-based sensors, although being highly sensitive, suffer from signal drift (20% drift ratio in f_r), a low Q factor of 8.6, and poor robustness to environmental interferences (or a low SIR of 18); and traditional dielectric-based sensors present disadvantages of a small frequency shift ratio $\Delta f_r / f_{r0}$ of 2% over full scale and a narrow working range (60 kPa) that is insufficient for orthodontic pressure sensing. The properties of the three types of sensors are compared in Table 1.

Overall, we provide a wireless sensing technology that can accurately measure pressure and torque over a broad range. Although we demonstrated only orthodontic pressure and torque measurement in this work, the polyelectrolyte-based wireless and drift-free LC sensors are expected to be used in many other applications, including wearables for health care, robot haptics, and consumer electronics.

MATERIALS AND METHODS

Synthesis of P(VBIM-TFSI) polyelectrolyte

For the synthesis of the polyelectrolyte, 2.0 g of [VBIM][TFSI] (99%; Adamas) was blended without (noncrosslinked) or with (crosslinked) 0.5 g of crosslinker TDE (Aladdin, 98%), along with 0.02 g of ethyl phenyl(2,4,6-trimethylbenzoyl) phosphinate (Macklin, 97%) serving as the initiator. The precursor mixture in each group was thoroughly stirred and shaken for 2 min. Next, the precursor of the polyelectrolyte was casted in a mold, which was created by placing a 0.1-mm-thick PDMS spacer between two pieces of polyethylene substrates. The precursor was cured under ultraviolet light (Analytik Jena, UVP CL-1000 Crosslinker) for 1 hour. After curing, the cured polyelectrolyte was immersed in alcohol for 5 min to remove unreacted monomers.

Synthesis of micro-structured PVDF-HFP/[EMIM][TFSI] ionogel

PVDF-HFP (Arkema, Kynar Flex 2801) of 1.0 g was dissolved in 9.0 g of acetone and stirred at 80°C for 30 min. Next, 3.0 g of [EMIM][TFSI] (99%; Aladdin) was added to the mixture and stirred for another 30 min at 80°C. The mixture was then casted on an Ecoflex 00-30 template with microstructures templated from an abrasive paper, cured at room temperature for 2 hours, and heated at 40°C for 2 hours for acetone evaporation. Last, the microstructured PVDF-HFP ionogel was peeled off from the template.

Structural, mechanical, and electrical characterization of polyelectrolyte

The chemical information of the polyelectrolytes was characterized using the following methods. First, wide-angle x-ray scattering was performed using a Xeuss 2.0 system (Xenocs) with a Cu-Kα x-ray source (wavelength: 0.154 nm). The scattering patterns were detected using a Pilatus 300K detector with a pixel size of 172 μm, and the sample-to-detector distance was set to be 88 mm. Raw data were processed using Foxtrot software. The glass transition temperatures of the polyelectrolytes were characterized using differential scanning calorimetry characterization (NETZSCH DSC214) under a nitrogen atmosphere, with a gas flow rate of 30 ml·min^{-1}. The temperature was increased from −80° to 200°C at a rate of 10°C·min^{-1}. All mechanical characterizations were conducted using an Instron E1000NL mechanical testing machine equipped with a 500 N of load cell, unless stated otherwise. For the tension test, specimens were prepared in a dumbbell shape with a width of 2.0 mm and a thickness of 1.0 mm to record their stress-strain curves. The applied force was measured by the aforementioned force gauge at a strain rate of 50 mm min^{-1}. In the compression test, samples were shaped

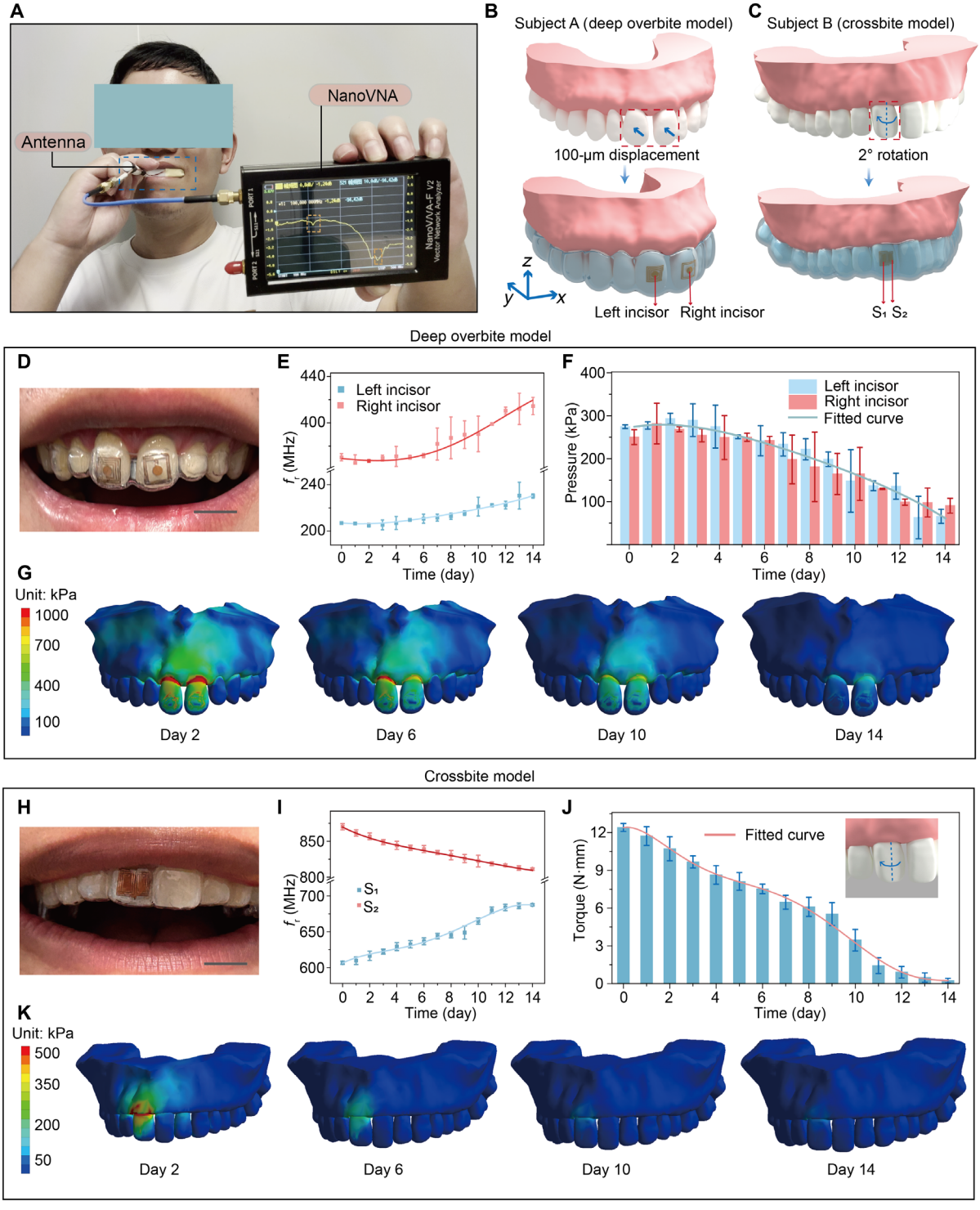

Fig. 5. In vivo orthodontic pressure and torque measurement. (**A**) Sensory system for orthodontic pressure and torque measurement. A nanoVNA was used to measure the S_{11} spectrum for portability purpose. (**B** and **C**) Diagram of the two subjects with (B) overbite and (C) crossbite tooth conditions. (**D**) Photograph of subject A wearing an aligner with two LC pressure sensors on the two incisors. Scale bar, 1 cm. (**E** and **F**) Orthodontic pressure measurement of the two incisors of subject A over 14 days during overbite treatment. Panel (E) shows the measured resonant frequencies of the two LC pressure sensors, and panel (F) shows the calculated orthodontic pressure over time. (**G**) Finite element analysis of stress distribution on the teeth and the alveolar bone of subject A during the overbite treatment. (**H**) Photograph of subject B wearing an aligner with a LC torque sensor on an incisor. Scale bar, 1 cm. (**I** and **J**) Orthodontic torque measurement over 14 days for crossbite treatment. Panel (I) shows the measured resonant frequencies of the LC torque sensor, and panel (J) shows the calculated orthodontic torque over time. (**K**) Finite element analysis of stress distribution on the teeth and the alveolar bone of subject B during the crossbite treatment.

Table 1. Comparison in sensing properties of polyelectrolyte-, ionogel-, and ion-free dielectric-based LC sensors. N, No; Y, yes.

Material	*Q* factor (tested under 140 kPa)	SIR	Sensing range	Drift ratio in frequency	$\Delta f_r/f_{r0}$	Suitable for orthodontic load test?
Ionogel	8.6	18	0–1 MPa	20%	13%	N
Polyelectrolyte	54	49	0–650 kPa	0.40%	28%	Y
Ion-free dielectric	76	31	0–60 kPa	6%	2%	N

into circular specimens with a diameter of 5 mm. A force control mode was used to maintain a stress level of 200 kPa for a duration of 10 hours, and the stress and strain data were recorded.

Electrochemical impedance spectroscopy measurement was performed using a perturbation of 5 mV over a frequency range of 1 Hz to 1 MHz on a CorrTest electrochemical workstation. The data were analyzed using ZView software to calculate the equivalent circuit. The sample was photocured in situ between two indium-tin oxide (ITO) glass substrates, with electrical connections established between the substrates and the electrochemical workstation. Dielectric loss data were measured using an Agilent E4991a instrument over a frequency range of 1 to 1000 MHz.

Processing and assembly of sensors

The microstructured template was first prepared by casting blended silicones of Ecoflex 00-30 and dragon skin 20 (Smooth-On) in a mass ratio of 3:2 onto a piece of commercial abrasive paper (#10000). After 10 hours, the cured silicone was carefully peeled off and used as the template for the formation of microstructured polyelectrolyte, which was cured by casting its precursor and exposed to ultraviolet light (Analytik Jena, UVP CL-1000 Crosslinker) for 1 hour. Afterward, the microstructured polyelectrolyte was cut to small circles with a diameter of 2 mm.

An LC sensor consisted of five layers: PDMS, PI-Cu, polyelectrolyte, PI-Cu, and PDMS. The coiled electrodes of PI-Cu (dimensions of 6 mm by 6 mm) were made using a laser cutter (laser wavelength: 355 nm; Beyond Laser) with a power of 2.8 kW and a scanning speed of 0.12 $m{\cdot}s^{-1}$. The patterned electrodes with coils were then transferred using a water transfer tape, with the PI side being plasma treated at 50 W for 30 s. The PDMS encapsulation layer was also plasma-treated in the same condition. The treated surfaces of the PI layer and PDMS were then bonded together and placed on a heating plate for 10 min for enhanced adhesion. The polyelectrolyte circle was placed on one half of the Cu-PI-PDMS layer and contacted to the Cu side of a PI-Cu electrode. The trilayer was then subjected to plasma treatment for 30 s and folded along its short middle axis to form a five-layered, bonded sensor (figs. S16 and S29).

Cytotoxicity characterization assay

An LC sensor of 20 mg in weight was incubated in 1.0 ml of Dulbecco's modified eagle medium (DMEM; Gibco, USA) supplemented with 10% fetal bovine serum (Gibco) and 1% penicillin/streptomycin (Gibco) for 24 hours at 37°C. An untreated DMEM medium was used as a control group. HAFs and HUVECs were seeded at a density of 5×10^4 cells per dish (three dishes per group) in confocal culture dishes with a diameter of 20 mm. The cell cultures were then placed in a 37°C incubator with 5% CO_2 for 24 hours. Cell viability was assessed using the LIVE/DEAD Viability/Cytotoxicity Assay Kit (Thermo Fisher Scientific) for mammalian cells. Laser confocal microscopy (SP8 Confocal) was used for excitation/emission imaging at 494 nm/517 nm and 517 nm/617 nm to visualize live cells. The number of live cells (stained with Calcium-AM) and dead cells (stained with PI) was determined using ImageJ 1.8.0 software to quantify cell viability.

Characterization of iontronic capacitors and LC sensors

The microstructures of P(VBIM-TFSI) polyelectrolyte and the cross section of the sensor were examined using scanning electron microscopy (Hitachi SU8230). Capacitance values of different sensors were measured using an inductance-capacitance-resistance (LCR) meter (E4980AL, Keysight) under 1.0 V and 1 kHz, unless otherwise noted.

The cyclic compression test of the sensors was conducted using a mechanical testing machine (Instron E1000NL). For static compression test, a 0.2-kg weight was placed on the sensors for a duration of 10 min or 10 hours. The capacitors were connected to the LCR meter to measure the capacitance over time. For wireless sensors, a VNA (E5071C, Keysight) with a flat pad antenna was used to collect the S_{11} spectrum with 1601 sweep points (fig. S30). The readout system (VNA) was powered by a battery or an alternating current. The sensors were attached to an aligner fragment with curved surfaces to mimic teeth (fig. S18). Curved antennas were used for data acquisition to test on tooth models and actual human teeth.

Wireless sensing in a tooth model

The measurement system consists of a VNA, a testing scaffold, a reading antenna, a computer, and a MATLAB application. The reading antenna was connected to the VNA with a coaxial transmission line, and the computer was linked to the VNA via a Virtual Instrument Software Architecture (VISA) interface. The S_{11} parameter measured by the VNA was recorded and calculated by the MATLAB application on the computer.

The aligners were created by hot pressing a tooth model without displacement or rotation. The LC sensors were fixed to the inner side of the aligner with silicone. The tooth models were categorized into three groups: The first group involved a single tooth with normal offset of 100, 150, 200, and 300 μm. The second group included a single tooth with rotations of 2°, 4°, 6°, and 8°. In the third group, six incisor teeth of the models displaced simultaneously with a normal offset of 200 μm. Data were collected using antennas fitted to the aligners, and each group underwent three tests, followed by statistical analysis.

Wireless sensing on human teeth

The tests on human teeth were approved by the Medical Ethics Committee of the Southern University of Science and Technology

under no. 20230098. The subjects were informed with the testing process and possible consequences, and all signed with an informed consent. No symptoms, such as oral ulcers, were found.

Subject A was with overbite. During the straightening, the teeth were gradually moved inward with a step of 100 μm. Subject B was with crossbite. During the treatment, the tooth was gradually rotated along the middle axis with a step of 2°. The NanoVNA system's read distance was about 1 cm, comparable to a traditional VNA. The antenna holder kept the lips apart during testing, ensuring accurate readout.

Patients wearing a plastic aligner was asked to remove the aligner during activities of eating and oral hygiene practices. The aligner was cleaned before wearing it again. Furthermore, our device was encapsulated in a PDMS layer, providing effective protection against food debris, ensuring that the sensor's internal components remain unaffected during operation. Data were collected at three specific time points a day via coil coupling.

Finite element analysis of dental orthodontics

Electromagnetic simulation software (Ansys Electronics Desktop, 2023) was used to simulate the S_{11} parameter of the sensors. A simplified oral model was constructed in the software, including alveolar bone, teeth, aligners, and sensors. The parameters of the organization are listed in table S2.

Mechanical simulation software (Ansys Workbench, 2021) was used to simulate the stress on teeth and alveolar bone during the orthodontic process. A simplified orthodontic model was built, including alveolar bone, tooth, and sensor, where the sensor was treated as a rigid body. The mechanical parameters of the components are shown in table S2. The mechanical data obtained from the orthodontic experiment were used as the initial condition input for the simulation.

Supplementary Materials

The PDF file includes:

Supplementary Text
Figs. S1 to S30
Tables S1 and S2
Legends for movies S1 to S8
References

Other Supplementary Material for this manuscript includes the following:

Movies S1 to S8

REFERENCES AND NOTES

1. S.-K. Kang, R. K. J. Murphy, S.-W. Hwang, S. M. Lee, D. V. Harburg, N. A. Krueger, J. Shin, P. Gamble, H. Cheng, S. Yu, Z. Liu, J. G. McCall, M. Stephen, H. Ying, J. Kim, G. Park, R. C. Webb, C. H. Lee, S. Chung, D. S. Wie, A. D. Gujar, B. Vemulapalli, A. H. Kim, K.-M. Lee, J. Cheng, Y. Huang, S. H. Lee, P. V. Braun, W. Z. Ray, J. A. Rogers, Bioresorbable silicon electronic sensors for the brain. *Nature* **530**, 71–76 (2016).
2. C. Ye, H. Lukas, M. Wang, Y. Lee, W. Gao, Nucleic acid-based wearable and implantable electrochemical sensors. *Chem. Soc. Rev.* **53**, 7960–7982 (2024).
3. C. M. Boutry, L. Beker, Y. Kaizawa, C. Vassos, H. Tran, A. C. Hinckley, R. Pfattner, S. Niu, J. Li, J. Claverie, Z. Wang, J. Chang, P. M. Fox, Z. Bao, Biodegradable and flexible arterial-pulse sensor for the wireless monitoring of blood flow. *Nat. Biomed. Eng.* **3**, 47–57 (2019).
4. R. Herber, H.-R. Lim, B. Rigo, W.-H. Yeo, Fully implantable wireless batteryless vascular electronics with printed soft sensors for multiplex sensing of hemodynamics. *Sci. Adv.* **8**, eabm1175 (2022).
5. Y. Li, W. Zhang, C. Zhao, W. Li, E. Dong, M. Xu, H. Huang, Y. Yang, L. Li, L. Zheng, M. Mao, S. Yao, L. Wang, J. Ma, X. Wang, W. Huang, Breaking the saturation of sensitivity for ultrawide range flexible pressure sensors by soft-strain effect. *Adv. Mater.* **36**, 2405405 (2024).
6. J. Deng, H. Yuk, J. Wu, C. E. Varela, X. Chen, E. T. Roche, C. F. Guo, X. Zhao, Electrical bioadhesive interface for bioelectronics. *Nat. Mater.* **20**, 229–236 (2021).
7. N. Li, Y. Li, Z. Cheng, Y. Liu, Y. Dai, S. Kang, S. Li, N. Shan, S. Wai, A. Ziaja, Y. Wang, J. Strzalka, W. Liu, C. Zhang, X. Gu, J. A. Hubbell, B. Tian, S. Wang, Bioadhesive polymer semiconductors and transistors for intimate biointerfaces. *Science* **381**, 686–693 (2023).
8. J. Deng, J. Wu, X. Chen, T. L. Sarrafian, C. E. Varela, W. Whyte, C. F. Guo, E. T. Roche, L. G. Griffiths, H. Yuk, C. S. Nabzdyk, X. Zhao, A bioadhesive pacing lead for atraumatic cardiac monitoring and stimulation in rodent and porcine models. *Sci. Transl. Med.* **16**, eado9003 (2024).
9. F. Elkholy, S. Weber, S. Repky, R. Jäger, F. Schmidt, B. G. Lapatki, Are aligners capable of inducing palatal bodily translation or palatal root torque of upper central incisors? A biomechanical in vitro study. *Clin. Oral. Invest.* **27**, 4289–4300 (2023).
10. A. D. Vardimon, D. Robbins, T. Brosh, In-vivo von mises strains during invisalign treatment. *Am. J. Orthod. Dentofac. Orthop.* **138**, 399–409 (2010).
11. L. J. Barbagallo, G. Shen, A. S. Jones, M. V. Swain, P. Petocz, M. A. Darendeliler, A novel pressure film approach for determining the force imparted by clear removable thermoplastic appliances. *Ann. Biomed. Eng.* **36**, 335–341 (2008).
12. Y. Midorikawa, H. Takemura, H. Mizoguchi, K. Soga, M. Kamimura, K. Suga, "Six-axis orthodontic force and moment sensing system for dentist technique training," in *Proceedings of the 38th Annual International Conference of the IEEE Engineering in Medicine and Biology Society* (IEEE, 2016), pp. 2206–2209.
13. M. S. Mannoor, H. Tao, J. D. Clayton, A. Sengupta, D. L. Kaplan, R. R. Naik, N. Verma, F. G. Omenetto, M. C. McAlpine, Graphene-based wireless bacteria detection on tooth enamel. *Nat. Commun.* **3**, 763 (2012).
14. Y. He, Y. Cheng, C. Yang, C. F. Guo, Creep-free polyelectrolyte elastomer for drift-free iontronic sensing. *Nat. Mater.* **23**, 1107–1114 (2024).
15. Y.-M. Yuan, B. Liu, M. R. Adibeig, Q. Xue, C. Qin, Q.-Y. Sun, Y. Jin, M. Wang, C. Yang, Microstructured polyelectrolyte elastomer-based ionotronic sensors with high sensitivities and excellent stability for artificial skins. *Adv. Mater.* **36**, e2310429 (2023).
16. V. Kalidasan, X. Yang, Z. Xiong, R. R. Li, H. Yao, H. Godaba, S. Obuobi, P. Singh, X. Guan, X. Tian, S. A. Kurt, Z. Li, D. Mukherjee, R. Rajarethinam, C. S. Chong, J.-W. Wang, P. L. R. Ee, W. Loke, B. C. K. Tee, J. Ouyang, C. J. Charles, J. S. Ho, Wirelessly operated bioelectronic sutures for the monitoring of deep surgical wounds. *Nat. Biomed. Eng.* **5**, 1217–1227 (2021).
17. J. Kim, J. Park, Y.-G. Park, E. Cha, M. Ku, H. S. An, K.-P. Lee, M.-I. Huh, J. Kim, T.-S. Kim, D. W. Kim, H. K. Kim, J.-U. Park, A soft and transparent contact lens for the wireless quantitative monitoring of intraocular pressure. *Nat. Biomed. Eng.* **5**, 772–782 (2021).
18. S. Niu, N. Matsuhisa, L. Beker, J. Li, S. Wang, J. Wang, Y. Jiang, X. Yan, Y. Yun, W. Burnett, A. S. Y. Poon, J. B.-H. Tok, X. Chen, Z. Bao, A wireless body area sensor network based on stretchable passive tags. *Nat. Electron.* **2**, 361–368 (2019).
19. W. Yang, S. Lin, W. Gong, R. Lin, C. Jiang, X. Yang, Y. Hu, J. Wang, X. Xiao, K. Li, Q. Yaogang Li, J. S. Zhang, Y. Ho, C. H. Liu, H. Wang, Single body-coupled fiber enables chipless textile electronics. *Science* **384**, 74–81 (2024).
20. S. H. Kim, A. Basir, R. Avila, J. Lim, S. W. Hong, G. Choe, J. H. Shin, J. H. Hwang, S. Y. Park, J. Joo, C. Lee, J. Choi, B. Lee, K.-S. Choi, S. Jung, T. Kim, H. Yoo, Y. H. Jung, Strain-invariant stretchable radio-frequency electronics. *Nature* **629**, 1047–1054 (2024).
21. B. Gleich, I. Schmale, T. Nielsen, J. Rahmer, Miniature magneto-mechanical resonators for wireless tracking and sensing. *Science* **380**, 966–971 (2023).
22. Y. Wu, Y. Liu, Y. Zhou, Q. Man, C. Hu, W. Asghar, F. Li, Z. Yu, J. Shang, G. Liu, M. Liao, R.-W. Li, A skin-inspired tactile sensor for smart prosthetics. *Sci. Robot.* **3**, eaat0429 (2018).
23. R. Lin, H.-J. Kim, S. Achavananthadith, S. A. Kurt, S. C. C. Tan, H. Yao, B. C. K. Tee, J. K. W. Lee, J. S. Ho, Wireless battery-free body sensor networks using near-field-enabled clothing. *Nat. Commun.* **11**, 444 (2020).
24. L. Y. Chen, B. C.-K. Tee, A. L. Chortos, G. Schwartz, V. Tse, D. J. Lipomi, H.-S. P. Wong, M. V. McConnell, Z. Bao, Continuous wireless pressure monitoring and mapping with ultra-small passive sensors for health monitoring and critical care. *Nat. Commun.* **5**, 5028 (2014).
25. Y. Chang, L. Wang, R. Li, Z. Zhang, Q. Wang, J. Yang, C. F. Guo, T. Pan, First decade of interfacial iontronic sensing: From droplet sensors to artificial skins. *Adv. Mater.* **33**, e2003464 (2021).
26. N. Bai, L. Wang, Q. Wang, J. Deng, Y. Wang, P. Lu, J. Huang, G. Li, Y. Zhang, J. Yang, K. Xie, X. Zhao, C. F. Guo, Graded intrafillable architecture-based iontronic pressure sensor with ultra-broad-range high sensitivity. *Nat. Commun.* **11**, 209 (2020).
27. J. Day, D. Geddis, J. Kim, S. H. Choi, H. Yoon, K. D. Song, Review of radio wave for power transmission in medical applications with safety. *Proc. SPIE* **9434**, 94340T (2015).
28. V. Schillaci, G. Stabile, A. Arestia, G. Shopova, A. Agresta, A. Salito, C. M. Giannitti, A. Natalizia, A. De Simone, F. Solimene, Dielectric-based tissue thickness measured during radiofrequency catheter ablation. *J. Cardiovasc. Electr.* **33**, 1587–1589 (2022).
29. G. Shin, W. Kim, M. C. Kim, J. Kim, J.-Y. Chung, J. Nah, A deionized water-infilled dual-layer insulator-applied brain-implanted uwb antenna for wireless biotelemetry applications. *IEEE Trans. Antennas Propag.* **70**, 6469–6478 (2022).

30. M. A. Ali, S. K. Mohideen, N. Vedachalam, Current status of underwater wireless communication techniques: A review, In *Proceedings of the 2022 Second International Conference on Advances in Electrical, Computing, Communication and Sustainable Technologies (ICAECT)* (IEEE, 2022).
31. H. Chen, A. S. Lou, A study of rf power attenuation in bio-tissues. *J. Med. Biol. Eng.* **24**, 141–146 (2004).
32. E. Istif, H. Mirzajani, Ç. Dağ, F. Mirlou, E. Y. Ozuaciksoz, C. Cakır, H. C. Koydemir, I. Yilgor, E. Yilgor, L. Beker, Miniaturized wireless sensor enables real-time monitoring of food spoilage. *Nat. Food* **4**, 427–436 (2023).
33. C. Li, J. Cheng, Y. He, X. He, Z. Xu, Q. Ge, C. Yang, Polyelectrolyte elastomer-based ionotronic sensors with multi-mode sensing capabilities via multi-material 3d printing. *Nat. Commun.* **14**, 4853 (2023).
34. S. N. Karobi, T. L. Sun, T. Kurokawa, F. Luo, T. Nakajima, T. Nonoyama, J. P. Gong, Creep behavior and delayed fracture of tough polyampholyte hydrogels by tensile test. *Macromolecules* **49**, 5630–5636 (2016).
35. S. B. Aziz, T. J. Woo, M. F. Z. Kadir, H. M. Ahmed, A conceptual review on polymer electrolytes and ion transport models. *J. Sci. Adv. Mater. Dev.* **3**, 1–17 (2018).
36. Z. Li, J. Fu, X. Zhou, S. Gui, L. Wei, H. Yang, H. Li, X. Guo, Ionic conduction in polymer-based solid electrolytes. *Adv. Sci.* **10**, 2201718 (2023).
37. S. K. Sharma, J. Mor, Free volume mediated decoupling of ionic conduction from segmental relaxation leading to enhancement in ionic conductivity of polymer electrolytes at low temperatures. *ACS Macro Lett.* **13**, 1211–1217 (2024).
38. J. Wei, L. Zhu, Intrinsic polymer dielectrics for high energy density and low loss electric energy storage. *Prog. Polym. Sci.* **106**, 101254 (2020).
39. L. Zhu, Exploring strategies for high dielectric constant and low loss polymer dielectrics. *J. Phys. Chem. Lett.* **5**, 3677–3687 (2014).
40. M. Tripathi, S. K. Tripathi, Electrical studies on ionic liquid-based gel polymer electrolyte for its application in edlcs. *Ionics* **23**, 2735–2746 (2017).
41. T. Kolodiazhnyi, P. Pulphol, W. Vittayakorn, N. Vittayakorn, Giant suppression of dielectric loss in $BaZrO_3$. *J. Eur. Ceram. Soc* **39**, 4144–4148 (2019).
42. T. O'Haver, *A pragmatic introduction to signal processing* (CreateSpace Press, 2018).
43. R. Nopper, R. Niekrawietz, L. Reindl, Wireless readout of passive lc sensors. *IEEE Trans. Instrum. Meas.* **59**, 2450–2457 (2010).
44. M. Klähn, C. Stüber, A. Seduraman, P. Wu, What determines the miscibility of ionic liquids with water? identification of the underlying factors to enable a straightforward prediction. *J. Phys. Chem. B.* **114**, 2856–2868 (2010).
45. J. G. Huddleston, A. E. Visser, W. M. Reichert, H. D. Willauer, G. A. Brokera, R. D. Rogers, Characterization and comparison of hydrophilic and hydrophobic room temperature ionic liquids incorporating the imidazolium cation. *Green Chem.* **3**, 156–164 (2001).
46. H. Kou, L. Zhang, Q. Tan, G. Liu, H. Dong, W. Zhang, J. Xiong, Wireless wide-range pressure sensor based on graphene/pdms sponge for tactile monitoring. *Sci. Rep.* **9**, 3916 (2019).
47. B. Nie, R. Huang, T. Yao, Y. Zhang, Y. Miao, C. Liu, J. Liu, X. Chen, Textile-based wireless pressure sensor array for human-interactive sensing. *Adv. Funct. Mater.* **29**, 1808786 (2019).
48. W. J. Deng, L. F. Wang, L. Dong, Q. A. Huang, Lc wireless sensitive pressure sensors with microstructured pdms dielectric layers for wound monitoring. *IEEE Sens. J.* **18**, 4886–4892 (2018).
49. J. Kim, M. Kim, M. S. Lee, K. Kim, S. Ji, Y. T. Kim, J. Park, K. Na, K. H. Bae, H. K. Kim, F. Bien, C. Y. Lee, J. U. Park, Wearable smart sensor systems integrated on soft contact lenses for wireless ocular diagnostics. *Nat. Commun.* **8**, 14997 (2017).
50. P. J. Chen, S. Saati, R. Varma, M. S. Humayun, Y. C. Tai, Wireless intraocular pressure sensing using microfabricated minimally invasive flexible-coiled lc sensor implant. *J. Microelectromech. S.* **19**, 721–734 (2010).
51. K. Liu, Y. Qin, G. Wu, D. Wang, H. Zhang, W. Wang, Y. Yuan, L. Gao, Iontronic capacitance-enhanced wireless passive pressure sensor for high-performance flexible sensing. *Appl. Phys. Lett.* **123**, 083501 (2023).
52. F. Nikbakhtnasrabadi, E. S. Hosseini, S. Dervin, D. Shakthivel, R. Dahiya, Smart bandage with inductor-capacitor resonant tank based printed wireless pressure sensor on electrospun poly-lactide nanofibers. *Adv. Electron. Mater.* **8**, 1–11 (2022).
53. T. Kim, A. H. Kalhori, T. H. Kim, C. Bao, W. S. Kim, 3d designed battery-free wireless origami pressure sensor. *Microsyst. Nanoeng.* **8**, 120 (2022).
54. F. Nikbakhtnasrabadi, E. S. Hosseini, R. Dahiya, Flexible strain sensor based on printed lc tank on electrospun piezoelectric nanofibers, in *Proceedings of the 2021 IEEE International Conference on Flexible and Printable Sensors and Systems* (IEEE, 2021), pp. 1–3.
55. A. Bulbul, H. Kim, Pressure sensor embedded inductive coil toward a wireless pressure sensing stent. *J. Microelectromech. Syts.* **30**, 224–233 (2021).

Acknowledgments: We would like to express our gratitude to H. Wang, T. Huang, and Y. Jiang from the Southern University of Science and Technology for their inspiring discussions. **Funding:** This work was supported by the National Natural Science Foundation of China (nos. T2225017 and 52073138); the Science, Technology, and Innovation Commission of Shenzhen Municipality (ZDSYS20210623092005017); the Science Technology and Innovation Committee of Shenzhen Municipality (no. JCYJ20241202125402004); the Shenzhen Sci-Tech Fund (no. YTDPT20181011104007); the Guangdong Provincial Key Laboratory Program (no. 2021B1212040001); the Climbing Program Special Funds (no. pdjh2024b330); and the Guangdong Basic and Applied Basic Research Foundation (2021A1515110862). **Author contributions:** Conceptualization: C.F.G. and J.So. Methodology: J.So., R.Y., J.Si., and X.C. Investigation: J.So., R.Y., S.X., Z.L., Y.F., and R.Z. Visualization: R.Y. and J.S. Supervision: C.F.G. and T.T.Y. Writing—original draft: R.Y. and J.So. Writing—review and editing: C.F.G. and T.T.Y. **Competing interests:** The authors declare that they have no competing interests. **Data and materials availability:** The MATLAB code for recording data from the VNA is available on Zenodo at https://doi.org/10.5281/zenodo.14625362, and the data are on Figshare at https://doi.org/10.6084/m9.figshare.28365911. All data needed to evaluate the conclusions in the paper are present in the paper and/or the Supplementary Materials.

Submitted 13 November 2024
Accepted 7 February 2025
Published 14 March 2025
10.1126/sciadv.adu6086